Strongly Interaction-Enhanced Valley Magnetic Response in Monolayer WSe_{2}

Zefang Wang, Kin Fai Mak, and Jie Shan

Phys. Rev. Lett. **120**, 066402 — Published 8 February 2018

DOI: 10.1103/PhysRevLett.120.066402

Strongly interaction-enhanced valley magnetic response in monolayer WSe_2

Zefang Wang[1,2], Kin Fai Mak[1,2,3]*, and Jie Shan[1,2,3]*

[1] Department of Physics and Center for 2-Dimensional and Layered Materials, The Pennsylvania State University, University Park, Pennsylvania 16802-6300, USA
[2] School of Applied and Engineering Physics and Department of Physics, Cornell University, Ithaca, New York 14853, USA
[3] Kavli Institute at Cornell for Nanoscale Science, Ithaca, New York 14853, USA

*E-mails: km627@cornell.edu; js3469@cornell.edu

Abstract

We have measured the doping dependence of the valley Zeeman splitting of the fundamental optical transitions in monolayer WSe_2 under an out-of-plane magnetic field by optical reflection contrast and photoluminescence spectroscopy. A nonlinear valley Zeeman effect, correlated with an over fourfold enhancement in the g-factor, has been observed. The effect occurs when the Fermi level crosses the spin-split upper conduction band, corresponding to a change of the spin-valley degeneracy from two to four. The enhancement increases and shows no sign of saturation as the sample temperature decreases. Our result demonstrates the importance of the Coulomb interactions in the valley magnetic response of two-dimensional transition metal dichalcogenide semiconductors.

Electrons in monolayer transition metal dichalcogenides (TMDs) with a honeycomb lattice structure possess a two-fold valley degree of freedom, corresponding to the K and K' point of the Brillouin zone [1-3]. Because of the strong spin-orbit interaction, the bands at the two valleys are spin split with the valley and spin locked to satisfy the time reversal symmetry [1-3] (Fig. 1a). Similar to the spin, the valley carries a magnetic moment and has been proposed as a new type of information carriers [1,4]. Several new valley-dependent phenomena, including the valley contrasting optical selection rules [5-9], valley Zeeman effect [10-15] and valley Hall effect [16,17], have emerged in the independent-particle picture and provided means to manipulate the valley polarization. In particular, the valley exciton splitting in an out-of-plane magnetic field has been shown to depend linearly on the field up to 65 Tesla [15], and a g-factor around four for neutral excitons and a similar to slightly larger g-factor for charged excitons have been reported for various monolayer TMDs [10-15,18]. On the other hand, even in the relatively high-density regime ($\sim 5 \times 10^{12}$ cm^{-2}), electrons in monolayer TMDs are strongly interacting with the Coulomb repulsion energy (~ 100's meV) dominating all other energy scales (both Fermi energy and conduction band spin splitting at K/K' are ~ 10's meV in WSe_2) [18]. An enhancement of the valley magnetic response by the strong electron-electron interaction effects has been recently reported in atomically thin TMDs [19-21]. A unique scenario arises when the Fermi level crosses the spin-split upper conduction band in TMDs (Fig. 1a), where the spin-valley degeneracy $l_s l_v$ changes from 2 to 4 (l_s and l_v stand for the spin and valley degeneracy, respectively) [18]. This provides a strongly interacting electron system with tunable internal degrees of freedom.

In this work, we study the valley Zeeman effect in monolayer WSe_2 over a wide electron doping range by both the reflection contrast and photoluminescence (PL) spectroscopy on dual-gated field-effect devices. We observe a strongly enhanced valley magnetic response of the fundamental optical transitions at low temperatures, accompanied by a nonlinear magnetic field dependence, when the spin-valley degeneracy doubles. The enhancement shows no sign of saturation as the sample temperature decreases. The observation can be understood as a consequence of a sharp increase in the exchange interaction when the number of electron species doubles [22-25]. Our results are in marked contrast to earlier studies on multi-valley Si and AlAs quantum wells (QWs), in which the interaction-induced renormalization of the spin susceptibility lowers when the valley degeneracy doubles [26,27]. The difference could be originated from the unique coupled spin-valley band structure of monolayer TMDs as we discuss below. Our study opens up new possibilities beyond the conventional multi-valley semiconductor QWs [25-32] for exploring strongly interacting electron systems with multiple internal degrees of freedom.

In our experiment, monolayer WSe_2 is embedded in hexagonal boron nitride (hBN) substrates with few-layer graphene as both contact and gate electrodes (See Figure S1a for an image). Details on the device fabrication have been reported elsewhere [18,33]. In short, encapsulation of monolayer WSe_2 in hBN produces high-quality samples [18,33,34], and the use of dual local gates enables high doping densities. Both reflection contrast and PL measurements were performed in the Faraday geometry in an Attocube closed-cycle cryostat (attoDry1000) with a superconducting magnet. In the PL

measurements, a linearly polarized excitation beam centered at 532 nm was focused into a diffraction-limited spot on the sample by a microscope objective. The excitation power was kept around 100 μW to limit sample heating while sufficient PL counts can still be obtained for good signal-to-noise ratios. The PL was collected by the same objective, passed through polarization selection optics, and detected by a spectrometer equipped with a charge-coupled-device (CCD) camera. The typical integration time for each spectrum is 3 s. The left and right circularly polarized components of the PL were selected by a combination of a quarter-wave plate, half-wave plate and linear polarizer. The half-wave plate was mounted on a motorized rotator to rapidly switch the emission polarization from one handedness to the other. To minimize long-term drifts of the setup, the left- and right-handed PL spectra were collected within 10 s of each other. Such a design, together with the data analysis method discussed below, allowed us to measure the valley Zeeman effect in a magnetic field as low as ~ 10 mT, in contrast to several T's in typical experiments. The reflection contrast measurements were performed using the same setup with a super-continuum light source [18,35]. Although the reflection contrast and PL spectroscopy yield similar results, the PL avoids complications from the Pauli blocking effect in the high doping regime (see Supplementary Sect. 3 for details) and provides a more precise determination of the valley Zeeman splitting energy (E_Z) of the optical transitions due to its background-free nature. We will therefore focus on the PL results below and include the comparison of the two methods in Supplementary Sect. 3. Two devices have been studied and their results are consistent.

Figure 1 shows the basic characterization of monolayer WSe_2 at 5 K in the absence of a magnetic field (See Supplementary Sect. 1 for more details). Figure 1b is a contour plot of the PL spectra at varying electron densities n, and Fig. 1c is the doping dependence of the integrated PL intensity. The doping density ($0 - 1 \times 10^{13}$ cm^{-2}) was calibrated using the gate voltages based on a capacitance model [18,35]. In the top axis of Fig. 1c we express the density in terms of the Wigner-Seitz radius $r_S = \frac{1}{\sqrt{\pi n} a_B^*}$ (for fixed $l_s l_v$ =2). Here the effective Bohr radius $a_B^* = \epsilon \frac{m_0}{m_c} a_B$ is the Bohr radius a_B modified by the conduction band mass in units of the free electron mass ($m_c/m_0 \approx 0.4$ [36]) and the average background dielectric constant $\epsilon = \sqrt{\epsilon_\perp \epsilon_\parallel} \approx 4.15$ ($\epsilon_\perp \approx 2.5$ [18] and $\epsilon_\parallel \approx 6.9$ [37] are the out-of-plane and in-plane dielectric constant of hBN, respectively). The r_S parameter is a measure of the Coulomb repulsion energy in terms of the kinetic/Fermi energy. The large r_S (3.3 – 7.0) suggests the importance of the interaction effects. The PL spectra are dominated by a sharp emission feature of width Γ ~ 3 - 7 meV. It arises from the optical transitions between the upper conduction and upper valence bands that have the same spin [2,18,35] (Fig. 1a). Coulomb interactions between the optically excited electron-hole pairs and the electron liquid in the doped sample further modify the nature of the transitions, giving rise to trions [3,38-41] or Fermi polarons [38,39] (or intervalley plasmons [40,41]) in different doping regimes. Here we refer to them simply as charged excitons or the fundamental optical transitions because of the wide range of doping levels being studied here (see Supplementary Sect. 1 for extra data and discussions). This feature shows a negligible Stokes shift (Figure S6), thus excluding the possibility of emission from localized or trapped states [42]. Weaker emissions from shallow trapped states (with a peak intensity < 20% of the main emission peak and a Stokes shift of ~ 10

meV) are also visible in the PL spectra (e.g. the feature near 1.655 eV in Fig. 2a and S2). As the electron doping density increases, the emission redshifts due to many-body renormalization of the exciton binding energy and the quasiparticle band gap [38-41,43]. Density $n_0 \approx 6.4 \times 10^{12}$cm^{-2} (dashed line, Fig. 1c) is required to dope electrons into the upper conduction band. The value was determined from the onset of the band filling or the Pauli blocking effect on the reflection contrast spectrum (Fig. S6) [18,35]. The onset of the Pauli blocking effect is accompanied with a sharp increase in the PL intensity, presumably due to the rapid increase of the conduction band occupancy and the radiative recombination rate [35].

We study the valley magnetic response of monolayer WSe_2 as a function of doping density by measuring the polarization-resolved PL spectra up to 8 T. Figure 2a illustrates the spectra under -2 T for two representative electron densities 5.0×10^{12} ($< n_0$) and 8.6×10^{12}cm^{-2} ($> n_0$). The left- and right-handed components correspond to the transitions at the K' and K valleys, respectively, according to the valley-contrasting optical selection rules (Fig. 1a) [1]. An increase in the splitting energy E_Z and hence a larger valley magnetic response for the larger doping density are clearly observable. Because of the complex recombination process of the electron-hole pairs in the presence of a strongly interacting electron liquid, the PL spectra have an asymmetric lineshape and cannot be described by a simple analytic function [44]. To extract E_Z, we chose to compute the difference between the average peak energy of the right- and left-handed PL spectra. To focus on the main emission feature, we limited the spectral window of interest to have PL intensity above 20% of its peak value. The value of 20% was chosen to conveniently eliminate most contributions from the aforementioned shallow trapped states. The obtained results are largely insensitive to the precise choice of the baseline (Figure S5). In addition, although the PL lineshape changes with doping, it remains similar for the two components at any given doping density and magnetic field and is expected to have a negligible effect on the analysis of E_Z. The uncertainty for the peak energy obtained from such an analysis is estimated to be ~ $\Gamma/\sqrt{N}$, where N is the total PL count (which is ~ 5×10^5 for a typical integration time of 3 s for our highly luminescent samples). Figure 2b shows the results for E_Z under $\mu_0 H = 0$ and -2 T (μ_0 denoting the vacuum permeability). The uncertainty in E_Z is about $5 - 30$ μeV, which is much smaller than the emission linewidth Γ (i.e. super-spectral-resolution). A small offset (< 50 μeV) is present at $H = 0$, which is likely due to systematic errors in the selection of the light polarization. More details are provided in Supplementary Sect. 2. Analysis of the PL handedness or valley polarization is presented in Supplementary Sect. 4.

The magnetic field dependence of E_Z at 5 K is shown in Figure 3a for several representative doping densities. Before doping into the upper conduction band ($n = 4 \times 10^{12}$ and 5×10^{12} cm^{-2}), the dependences are linear for the field ranging from -8 T to 8 T. This is in agreement with earlier studies [10-15]. However, after doping into the upper conduction band (6.7×10^{12}, 7.0×10^{12} and 7.3×10^{12} cm^{-2}) the dependences become sub-linear with a kink at H^* (indicated by arrows). The H^* strength increases with doping density. For $n = 8.3 \times 10^{12}$ cm^{-2}, H^* is outside the measurement range and the dependence appears linear again. We extracted the g-factor from the slope of the $E_Z - H$

dependence at the origin $g_X = \frac{1}{\mu_B \mu_0} \frac{dE_Z}{dH}\Big|_{H=0}$, where $\mu_B \approx 0.0579$ meV/T is the Bohr magneton. We also estimated H^* by fitting the $E_Z - H$ dependences with a phenomenological expression $E_Z = g_X \mu_B \mu_0 H^* \tanh(H/H^*)$ (dashed lines, Fig. 3a). The doping dependence of $|g_X|$ (= -g_X) and H^* is depicted in Fig. 3b and 3c, respectively. For $n < n_0$ ($l_s l_v$ = 2), $|g_X|$ decreases slowly from ~ 5 to 3 with increasing n. The value is consistent with the reported values for charged excitons in monolayer WSe_2 [12-14]. The observed doping dependence of the g-factor may explain the variations among the reported values for samples with different levels of intentional or unintentional doping. For $n > n_0$ ($l_s l_v$ = 4), $|g_X|$ increases rapidly to ~ 12, and then decreases with further increase of n. At the same time, $\mu_0 H^*$ increases from ~ 4 T at n_0, followed by a linear dependence on $(n - n_0)$ (solid line, Fig. 3c). The departure from the linear dependence, as well as the broadening of the enhancement of $|g_X|$ near n_0, is likely due to Fermi level broadening by impurities, defects and sample inhomogeneities. The large g-factor observed here for the fundamental optical transition has a distinct origin from that of localized or trapped excitons seen in Fig. 2a and in Ref. [45-48]. The effect, an intrinsic property of monolayer WSe_2 tunable by electrostatic doping, is also different from that by proximity coupling to a ferromagnet in WSe_2/EuS heterostructures [49,50]. The PL handedness under finite magnetic fields also depends strongly on doping density. Details are discussed in Supplementary Sect. 4.

In the simple band picture, the total magnetic moment of a given band consists of the atomic orbital, inter-atomic orbital (or valley) and spin contributions [11,12]. In the two-band $k \cdot p$ model, the atomic orbital moments are $\pm 2\mu_B$ for the valence bands and 0 for the conduction bands near the K'/K point, reflecting the properties of the *d*-orbitals of the W atom that form the bands [1]. The inter-atomic orbital moments are $\pm \frac{m_0}{m_{v/c}} \mu_B$ for the K'/K point [11,12] with the Bohr magneton modified by the effective masses (m_c and m_v are the conduction band and valence band masses, respectively). The total magnetic moment of the upper conduction band and the upper valence band including the spin contribution μ_B are therefore $\mu_B(1 + \frac{m_0}{m_c})$ and $\mu_B(3 + \frac{m_0}{m_v})$, respectively, for the K' valley [12]. The magnetic moment of the K valley is of opposite sign by the time reversal symmetry. Ignoring the electron-electron interactions, the exciton valley splitting under magnetic field $\mu_0 H$ is determined by the difference between the valley Zeeman splitting of the conduction band and the valence band $E_Z = 2\mu_B \mu_0 H[-2 + \left(\frac{m_0}{m_c} - \frac{m_0}{m_v}\right)]$ [10-15]. In case of similar band masses such as in monolayer WSe_2, we obtain $E_Z \approx -4\mu_B \mu_0 H$ and $g_X \approx -4$. The result remains unchanged for charged excitons. Our observation of the nonlinear field dependence of the valley Zeeman splitting and the strong enhancement of the g-factor cannot be explained in this simple non-interacting picture.

Our experimental observation could be understood by invoking the strong interaction effects. In the vicinity of n_0, the Coulomb repulsion energy stays nearly unchanged ($r_S \approx 4.2$), but the exchange interaction, which is sensitive to the electron's internal degrees of freedom (spin-valley degeneracy) changes abruptly when the Fermi level crosses the upper conduction band. A dimensionless parameter $r_X = \sqrt{\frac{l_s l_v}{2}} r_S$ has

been suggested to characterize the strength of the exchange interaction in terms of the kinetic/Fermi energy [24,25]. In the inset of Fig. 3b we show the doping dependence of r_S and r_X in the vicinity of n_0, illustrating the difference between the two types of interactions. While a sudden increase in r_X could lead to an enhanced or weakened magnetic response depending on the sign of the exchange integral [24], our data shows that it favors a larger spin and valley polarization in monolayer WSe_2 (i.e. a larger Zeeman splitting and g-factor). The effect of the exchange field remains significant until the externally applied field reaches H^*, at which the electrons in the upper conduction band become fully spin and valley polarized (i.e. the Fermi level is at the bottom of the upper conduction band at one of the valleys). For $H > H^*$, the effect of the exchange field diminishes, resulting in sub-linear $E_Z - H$ dependences (Fig. 3a). One can relate H^* to n by $|g_c|\mu_B\mu_0 H^* = \frac{\hbar^2\pi}{m_c}(n - n_0)$ [25,29], where g_c is the upper conduction band valley g-factor, and equal masses for the upper and lower conduction bands have been used. A comparison with experiment (solid line in Fig. 3c) yields $m_c|g_c| \approx (4.7 \pm 0.1)m_0$. In the independent-particle picture, this factor is evaluated to be $m_c|g_c| \approx 2.8\, m_0$ using the conduction band valley g-factor $|g_c| = 2 + 2\frac{m_0}{m_c}$ [12] and $m_c \approx 0.4\, m_0$ [36]). The "non-interacting" value for the paramagnetic susceptibility ($\sim m_c|g_c|$) is smaller than the experimental value, in support of the interpretation of an interaction-enhanced magnetic response.

The large enhancement of $|g_X|$ upon doubling the spin-valley degeneracy in monolayer WSe_2 is opposite to the weakened magnetic response observed upon an increase in the valley degeneracy by application of strain or a magnetic field in conventional multi-valley QWs [26,27]. Two factors could contribute to the different behaviors. First are the distinct electronic bands. Monolayer WSe_2 is a Dirac system with strong spin-orbit interactions, whereas conventional multi-valley QWs have nearly spin-degenerate parabolic bands. Second, an increase of doping density near n_0 changes only r_X significantly in monolayer WSe_2, while an increase in the valley degeneracy in QWs changes both r_S and r_X [24,26,27]. Next, away from n_0 (both below and above), the weaker variation in $|g_X|$ could be related to the changing r_S. As doping increases, r_S decreases (i.e. interaction effects weaken) and so does $|g_X|$. This behavior is similar to the reported results on Si QWs [28,30,31] and is also in qualitative agreement with theoretical calculations [24,51]. Finally, the discussion above does not consider the electron-hole interactions, which are relevant for optical measurements and are known to be strong in monolayer TMDs. Further theoretical studies on the valley magnetic response of monolayer TMDs in the strongly interacting regime including the Dirac bands and the strong spin-orbit interactions are needed.

Finally, we briefly discuss the temperature dependence of $|g_X|$. Figure 4a shows the density dependence of $|g_X|$ determined from the valley Zeeman splitting at 2 T at temperatures ranging from 10 to 80 K. The strong enhancement in $|g_X|$ for $n > n_0$ emerges only at low temperatures (< 40 K). Figure 4b shows the temperature dependence of $|g_X|$ at two representative doping densities. For $n = 4.0 \times 10^{12} < n_0$, $|g_X|(\approx 4)$ is nearly temperature independent. On the other hand, for n slightly above n_0, $|g_X|$ grows significantly as temperature decreases. No sign of saturation is observed down to 5 K.

These results show that sufficiently small thermal broadening of the Fermi level is required to reveal the interaction-enhanced magnetic response. In addition, the absence of saturation in the enhancement of $|g_X|$ suggests that the magnetic response could be further enhanced at lower temperatures and in higher quality samples. In conclusion, our experiment has demonstrated the strong enhancement of the valley magnetic response in monolayer WSe_2 by the interaction effects through a systematic doping dependence study. The possibility of a ferromagnetic instability and a magnetically ordered ground state in monolayer TMDs remains open [22-24,51].

Acknowledgements

The research was supported by National Science Foundation DMR-1420451 for optical spectroscopy measurements, the US Department of Energy, Office of Basic Energy Sciences under award no. DESC0013883 for sample and device fabrication, and the US Department of Energy, Office of Basic Energy Sciences under award no. DESC0012635 (J.S.) and AFOSR under grant FA9550-16-1-0249 (K.F.M.) for data analysis. K.F.M. also acknowledges support from a David and Lucille Packard Fellowship and Sloan Fellowship.

References

[1] D. Xiao, G. B. Liu, W. X. Feng, X. D. Xu, and W. Yao, Phys. Rev. Lett. **108**, 196802 (2012).
[2] X. Xu, W. Yao, D. Xiao, and T. F. Heinz, Nat. Phys. **10**, 343 (2014).
[3] K. F. Mak and J. Shan, Nat. Photon. **10**, 216 (2016).
[4] D. Xiao, W. Yao, and Q. Niu, Phys. Rev. Lett. **99**, 236809 (2007).
[5] T. Cao *et al.*, Nat. Commun. **3**, 887 (2012).
[6] H. Zeng, J. Dai, W. Yao, D. Xiao, and X. Cui, Nat. Nano. **7**, 490 (2012).
[7] K. F. Mak, K. He, J. Shan, and T. F. Heinz, Nat. Nano. **7**, 494 (2012).
[8] G. Sallen *et al.*, Phys. Rev. B **86**, 081301 (2012).
[9] A. M. Jones *et al.*, Nat. Nano. **8**, 634 (2013).
[10] Y. L. Li *et al.*, Phys. Rev. Lett. **113**, 266804 (2014).
[11] D. MacNeill, C. Heikes, K. F. Mak, Z. Anderson, A. Kormanyos, V. Zolyomi, J. Park, and D. C. Ralph, Phys. Rev. Lett. **114**, 037401 (2015).
[12] G. Aivazian *et al.*, Nat. Phys. **11**, 148 (2015).
[13] A. Srivastava, M. Sidler, A. V. Allain, D. S. Lembke, A. Kis, and A. Imamoglu, Nat. Phys. **11**, 141 (2015).
[14] G. Wang, L. Bouet, M. M. Glazov, T. Amand, E. L. Ivchenko, E. Palleau, X. Marie, and B. Urbaszek, 2D Mater. **2**, 034002 (2015).
[15] A. V. Stier, K. M. McCreary, B. T. Jonker, J. Kono, and S. A. Crooker, Nat. Commun. **7**, 10643 (2016).
[16] K. F. Mak, K. L. McGill, J. Park, and P. L. McEuen, Science **344**, 1489 (2014).
[17] J. Lee, K. F. Mak, and J. Shan, Nat. Nano. **11**, 421 (2016).
[18] B. Huang *et al.*, Nature **546**, 270 (2017).

[19] P. Back, M. Sidler, O. Cotlet, A. Srivastava, N. Takemura, M. Kroner, and A. Imamoglu, Phys. Rev. Lett. **118,** 237404 (2017).
[20] S. Xu *et al.*, Phys. Rev. Lett. **118,** 067702 (2017).
[21] H. C. Movva, B. Fallahazad, K. Kim, S. Larentis, T. Taniguchi, K. Watanabe, S. K. Banerjee, and E. Tutuc, Phys. Rev. Lett. **118,** 247701 (2017).
[22] B. Tanatar and D. M. Ceperley, Phys. Rev. B **39**, 5005 (1989).
[23] C. Attaccalite, S. Moroni, P. Gori-Giorgi, and G. B. Bachelet, Phys. Rev. Lett. **88**, 256601 (2002).
[24] S. Das Sarma, E. H. Hwang, and Q. Li, Phys. Rev. B **80**, 121303 (2009).
[25] E. Abrahams, S. V. Kravchenko, and M. P. Sarachik, Rev. Mod. Phys. **73**, 251 (2001).
[26] Y. P. Shkolnikov, K. Vakili, E. P. De Poortere, and M. Shayegan, Phys. Rev. Lett. **92**, 246804 (2004).
[27] V. T. Renard *et al.*, Nat. Commun. **6**, 7230 (2015).
[28] F. F. Fang and P. J. Stiles, Phys. Rev. **174**, 823 (1968).
[29] A. A. Shashkin, S. V. Kravchenko, V. T. Dolgopolov, and T. M. Klapwijk, Phys. Rev. Lett. **87**, 086801 (2001).
[30] V. M. Pudalov, M. E. Gershenson, H. Kojima, N. Butch, E. M. Dizhur, G. Brunthaler, A. Prinz, and G. Bauer, Phys. Rev. Lett. **88**, 196404 (2002).
[31] A. A. Shashkin, S. V. Kravchenko, V. T. Dolgopolov, and T. M. Klapwijk, Phys. Rev. B **66**, 073303 (2002).
[32] Y. P. Shkolnikov, E. P. De Poortere, E. Tutuc, and M. Shayegan, Phys. Rev. Lett. **89**, 226805 (2002).
[33] X. Cui *et al.*, Nat. Nano. **10**, 534 (2015).
[34] B. Fallahazad, H. C. P. Movva, K. Kim, S. Larentis, T. Taniguchi, K. Watanabe, S. K. Banerjee, and E. Tutuc, Phys. Rev. Lett. **116**, 086601 (2016).
[35] C. Gong *et al.*, Nature **546**, 265 (2017).
[36] G.-B. Liu, W.-Y. Shan, Y. Yao, W. Yao, and D. Xiao, Phys. Rev. B **88**, 085433 (2013).
[37] R. Geick, C. H. Perry, and G. Rupprecht, Phys. Rev. **146**, 543 (1966).
[38] M. Sidler, P. Back, O. Cotlet, A. Srivastava, T. Fink, M. Kroner, E. Demler, and A. Imamoglu, Nat. Phys. **13**, 255 (2017).
[39] D. K. Efimkin and A. H. MacDonald, Phys. Rev. B **95**, 035417 (2017).
[40] H. Dery, Phys. Rev. B **94**, 075421 (2016).
[41] D. Van Tuan, B. Scharf, I. Žutić, and H. Dery, Phys. Rev. X **7**, 041040 (2017).
[42] Z. Wang, L. Zhao, K. F. Mak, and J. Shan, Nano Lett. **17**, 740 (2017).
[43] S. Gao, Y. Liang, C. D. Spataru, and L. Yang, Nano Lett. **16**, 5568 (2016).
[44] S. Schmitt-Rink, D. S. Chemla, and D. A. B. Miller, Adv. Phys. **38**, 89 (1989).
[45] A. Srivastava, M. Sidler, A. V. Allain, D. S. Lembke, A. Kis, and A. Imamoğlu, Nat. Nano. **10**, 491 (2015).
[46] M. Koperski, K. Nogajewski, A. Arora, V. Cherkez, P. Mallet, J. Y. Veuillen, J. Marcus, P. Kossacki, and M. Potemski, Nat. Nano. **10**, 503 (2015).
[47] Y.-M. He *et al.*, Nat. Nano. **10**, 497 (2015).
[48] C. Chakraborty, L. Kinnischtzke, K. M. Goodfellow, R. Beams, and A. N. Vamivakas, Nat. Nano. **10**, 507 (2015).
[49] C. Zhao *et al.*, Nat. Nano. **12**, 757 (2017).

[50] D. Zhong *et al.*, Sci. Adv. **3**, 1603113 (2017).
[51] Y. Zhang and S. Das Sarma, Phys. Rev. B **72**, 115317 (2005).
[52] See Supplementary Material [url] for supplementary data and analysis, which includes Refs. [53].
[53] Z. Wang, J. Shan, and K. F. Mak, Nat. Nano. **12**, 144 (2017).

Figure captions

Figure 1(a) Electronic band structure of monolayer WSe_2 at the K and K' valleys including the two spin-split conduction bands ($c1$, $c2$) and the upper valence band. Optical transitions at the K' and K valleys (allowed only between bands of the same spin) are coupled to the left and right circularly polarized light. (b) Contour plot of the photoluminescence (PL) counts as a function of photon energy and electron doping density n. The integration time is 3 s. (c) Spectrally integrated PL vs. doping density n (bottom axis) and Wigner-Seitz radius r_S (top axis). A sharp increase occurs around $n_0 \approx 6.4 \times 10^{12}$ cm^{-2} (dashed line) when the Fermi level crosses the upper conduction band.

Figure 2(a) Handedness-resolved PL spectra (normalized) at doping densities 5.0x10^{12} cm^{-2} (left) and 8.6x10^{12} cm^{-2} (right) under -2 T. (b) Valley Zeeman splitting as a function of doping density under 0 T and -2 T.

Figure 3(a) Valley Zeeman splitting of the fundamental optical transition as a function of magnetic field ranging from -8 T to 8 T at representative doping densities (vertically shifted for clarity). Solid color lines are experimental data and dashed black lines are fits to the experimental data using a phenomenological function described in the text. The field dependence has a kink at H^*. (b) Doping dependence of the g-factor. The error bars are estimated from the uncertainties of the PL peak energies. Dashed line denotes $n = n_0$, at which the Fermi level crosses the upper conduction band and the spin-valley degeneracy $l_s l_v$ changes from 2 to 4. The inset shows the doping dependence of r_S and r_X near n_0. (c) Doping dependence of H^*. The solid line is a linear fit to the experimental data (symbols) with an x-intercept at n_0.

Figure 4(a) The g-factor of the fundamental optical transition vs doping density at representative temperatures. (b) The g-factor vs temperature at representative doping densities. The g-factor values were determined from the Zeeman splitting at 2 T.

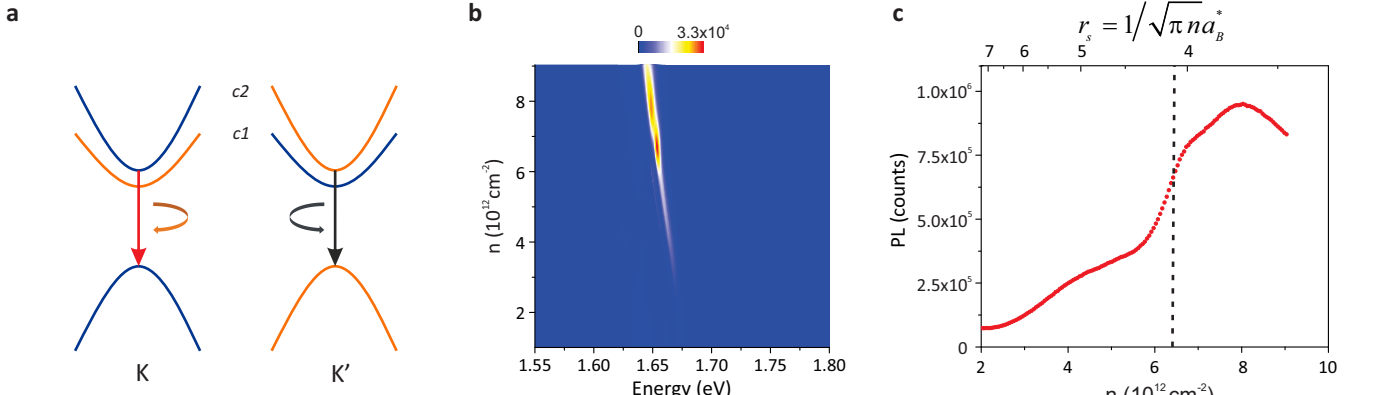
a
c2
c1
K
K'
b
0
3.3x10^4
n (10^12 cm^-2)
8
6
4
2
1.55
1.60
1.65
1.70
1.75
1.80
Energy (eV)
c
r_s = 1/√(πn) a_B^*
7
6
5
4
PL (counts)
1.0x10^6
7.5x10^5
5.0x10^5
2.5x10^5
0
2
4
6
8
10
n (10^12 cm^-2)

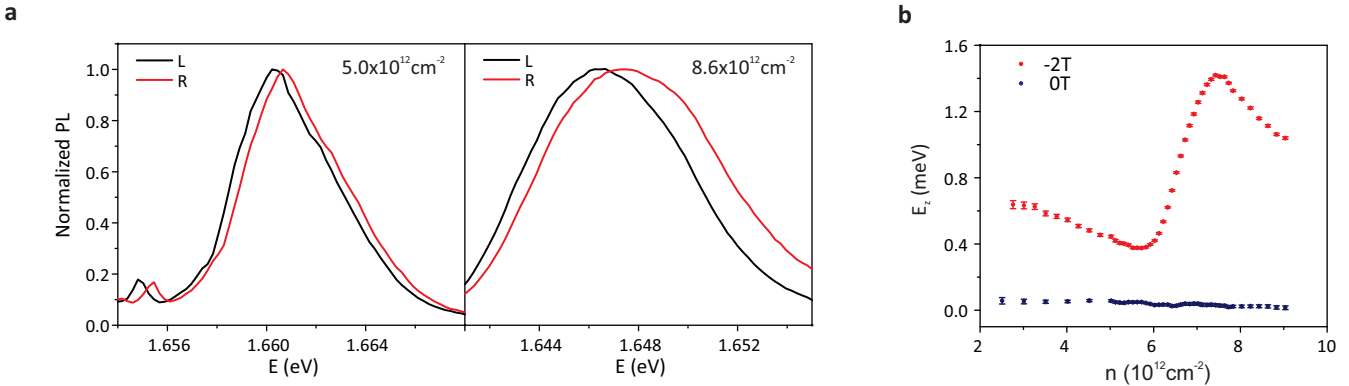
a
b
Normalized PL
L
R
5.0x10^12cm^-2
8.6x10^12cm^-2
E (eV)
E (eV)
-2T
0T
E_z (meV)
n (10^12cm^-2)

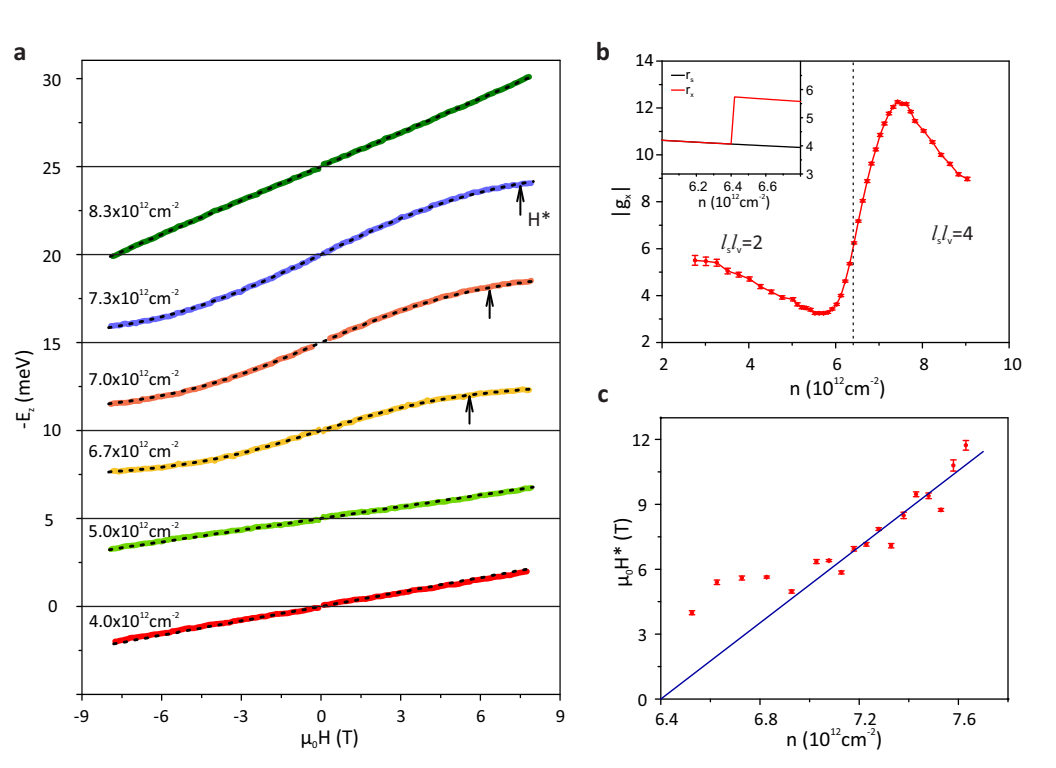
a
b
c
-E_z (meV)
μ_0H (T)
8.3x10^12cm^-2
7.3x10^12cm^-2
7.0x10^12cm^-2
6.7x10^12cm^-2
5.0x10^12cm^-2
4.0x10^12cm^-2
H*
|g_s|
n (10^12cm^-2)
l_s l_v=2
l_s l_v=4
r_s
r_x
μ_0H* (T)

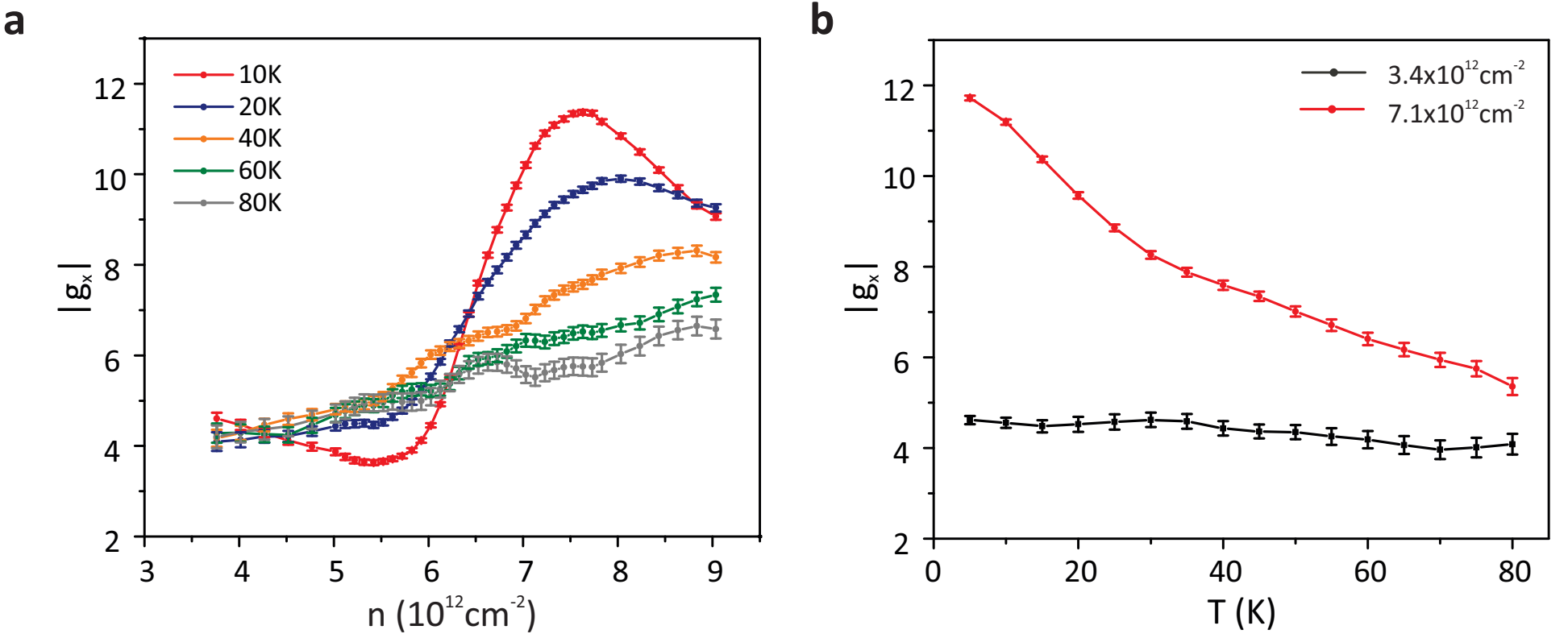
a
10K
20K
40K
60K
80K
|g_x|
n (10^12 cm^-2)
b
3.4x10^12 cm^-2
7.1x10^12 cm^-2
|g_x|
T (K)